Available online at www.sciencedirect.com
ScienceDirect
Earth and Planetary Science Letters 269 (2008) 164–174
EPSL
www.elsevier.com/locate/epsl

Element partitioning between magnesium silicate perovskite and ferropericlase: New insights into bulk lower-mantle geochemistry

Anne-Line Auzende [a,*], James Badro [a,b], Frederick J. Ryerson [b], Peter K. Weber [b], Stewart J. Fallon [b], Ahmed Addad [c], Julien Siebert [b], Guillaume Fiquet [a]

[a] IPGP, IMPMC, Université Paris VI & Paris VII, CNRS, Department of Mineralogy, campus Boucicaut, 140 rue de Lourmel, 75015 Paris, France
[b] LLNL, Energy and Environment, Experimental geophysics, University of California, Livermore, CA 94550, United States
[c] LSPES, CNRS, Université des Sciences et Technologies de Lille, Cité scientifique, 59655 Villeneuve d'Ascq, France

Received 12 July 2007; received in revised form 18 January 2008; accepted 3 February 2008
Available online 16 February 2008
Editor: G.D. Price

Abstract

In this study, we investigated iron–magnesium exchange and transition-metal trace-element partitioning between magnesium silicate perovskite (Mg,Fe)SiO_3 and ferropericlase (Mg,Fe)O synthetised under lower-mantle conditions (up to 115 GPa and 2200 K) in a laser-heated diamond anvil cell. Recovered samples were thinned to electron transparency by focused ion beam and characterized by analytical transmission electron microscopy (ATEM) and nanometer-scale secondary ion mass spectroscopy (nanoSIMS). Iron concentrations in both phases were obtained from X-ray energy dispersive spectroscopy measurements and nanoSIMS. Our results are the first to show that recently reported spin-state and phase transitions in the lower mantle directly affect the evolution of Fe–Mg exchange between both phases. Mg-perovskite becomes increasingly iron-depleted above 70–80 GPa possibly due to the high spin–low spin transition of iron in ferropericlase. Conversely, the perovskite to post-perovskite transition is accompanied by a strong iron enrichment of the silicate phase, ferropericlase remaining in the Fe-rich phase though. Nanoparticles of metallic iron were observed in the perovskite-bearing runs, suggesting the disproportionation of ferrous iron oxide, but were not observed when the post-perovskite phase was present. Implications on the oxidation state of the Earth and core segregation will be discussed. Transition trace-element (Ni, Mn) concentrations (determined with the nanoSIMS) show similar trends and could thus be used to trace the origin of diamonds generated at depth. This study provides new results likely to improve the geochemical and geophysical models of the Earth's deep interiors.

Keywords: high pressure; iron partitioning; perovskite; ferropericlase; post-perovskite; laser-heated diamond anvil cell; ATEM; nanoSIMS

1. Introduction

Seismological heterogeneities reveal a distinct region in the lower mantle between 1600 km to 2300 km depth (Van der Hilst et al., 1997) which is interpreted by Kellogg et al. (1999) as a compositionally dense layer. The underlying D″ layer is also likely to be a compositionally distinct layer characterized by anomalous seismic velocities at the base of the lower mantle (Wyesession et al., 1998). However, the origin of this deep stratification is still hotly debated. Recent works indicate that changes in the chemistry of iron such as the pressure-induced spin-state transitions (Badro et al., 2003) and variations in Mg/Fe ratios due to phase transitions (Kellogg et al., 1999; Mao et al., 2006) could be responsible for the deep mantle layering. Indeed, iron can strongly affect the physical and chemical properties of the high-pressure phases (McCammon, 1997; Andrault, 2001; Kieffer et al., 2002; Kung et al., 2002; Badro et al., 2003, 2004; Goncharov et al., 2006). Interpretations of geophysical and geochemical data are thus highly dependent on mineral compositions obtained at high pressures.

* Corresponding author. Tel.: +33 1 44 27 50 59; fax: +33 1 44 27 37 85.
E-mail addresses: auzende@impmc.jussieu.fr (A.-L. Auzende), badro@impmc.jussieu.fr (J. Badro), ryerson1@llnl.gov (F.J. Ryerson), weber21@llnl.gov (P.K. Weber), Fallon4@llnl.gov (S.J. Fallon), ahmed.addad@univ-lille1.fr (A. Addad), siebert2@llnl.gov (J. Siebert), fiquet@impmc.jussieu.fr (G. Fiquet).

0012-821X/$ - see front matter © 2008 Elsevier B.V. All rights reserved.
doi:10.1016/j.epsl.2008.02.001

High-pressure experiments coupled to seismological observations lead to the widely accepted idea that the lower mantle consists of about 80 wt.% of magnesian perovskite $(Mg,Fe)SiO_3$ (thereafter called *pv*), 15 wt.% of ferropericlase (Mg,Fe)O (*fp*) and 5 wt.% of calcium perovskite $CaSiO_3$ [e.g. Wood, 2000]. Recently, Murakami et al. (2004) have shown that pv transforms into a post-perovskite (*ppv*) phase in the lowermost part of the mantle. The chemical and physical properties of these high-pressure phases were intensively investigated and show an important compositional dependence, mainly with iron content as previously mentioned (Dobson and Brodholt, 2000; Kieffer et al., 2002; Jackson et al., 2006). The Fe–Mg exchange between pv and fp at high pressures and temperatures has been extensively studied because of its implications for the composition and dynamics of the lower mantle. However, there is no consensus on the value of that coefficient [e.g. Mao et al., 1997]. Among the potential sources of this disparity, the difficulty in obtaining high-quality chemical analyses on high-pressure samples may be the most significant [e.g. Fujino et al., 2004]. Lower-mantle conditions ($P>25$ GPa, $T>2000$ K) are achieved in diamond anvil cell devices coupled to infrared laser heating (LH-DAC) and the recovered samples do not exceed a few tens of microns in diameter with a thickness of a few microns. The grain size within these high-pressure samples (<1 μm) precludes the use of classical chemical analysis tools (electron probe, mass spectroscopy…). Until recently, the determination of chemical compositions of lower-mantle phases was indirectly inferred (X-ray diffraction) from the relationship of unit-cell volumes and composition (Mao et al., 1997; Andrault, 2001). Results achieved by analytical transmission electron microscopy (ATEM) are at odds with exchange coefficient obtained by the previous method (Martinez et al., 1997; Kesson et al., 2002; Kobayashi et al., 2005). The presence of aluminium strongly influences the partition behaviour of iron, increasing the exchange coefficient in favour of pv (Murakami et al., 2005). Finally, extrapolation of high-accuracy lower pressure (<25 GPa) data to higher pressures cannot account for the effects of pressure-induced transformations such as spin or phase transitions (Badro et al., 2003, 2004; Murakami et al., 2004).

In this paper, we reinvestigate the distribution of iron between pv (or ppv) and fp covering the lower-mantle P–T conditions in a simple Al-free system. The starting material San Carlos olivine was equilibrated in a LH-DAC at lower-mantle conditions. An electron-transparent thin section was then extracted from the bulk DAC sample by the focused ion beam technique (FIB). These thin sections were then analysed by ATEM (for major-element chemistry and mineralogy). Elemental abundances at all concentration levels were then measured by nanoscale secondary ion mass spectrometry (nanoSIMS).

2. Experimental procedure

2.1. High pressure–high temperature synthesis

Single crystals of San Carlos olivine ($[(Mg_{1.8}Fe_{0.2})SiO_4]$ by electron microprobe analysis) were used as starting material for experiments at pressures ranging from 55 to 78 GPa. At higher pressures, after failing to obtain grain size larger than 100 nm with single crystal starting materials, we ground the olivine in an agate mortar. The syntheses were conducted with a Mao-Bell type diamond anvil cell (DAC) equipped with 150 or 100 μm-culet bevelled diamonds. The confining gasket, made of a 200 μm thick rhenium foil, was pre-indented to 30 μm. A 80 μm-hole was then drilled into the gasket. Olivine was loaded into the pressure chamber together with a ruby chip used as a pressure calibrant (Mao et al., 1986). No pressure medium was used but our sampling method (see Section 2.2) made that point not critical. The samples were first compressed to the required pressure at room temperature. Next, they were heated at high pressure by focusing a single-mode TEM_{00} Nd:YAG laser beam ($\lambda=1064$ nm–20 W) to a spot of 30 μm in diameter. Temperature was measured by the spectro-radiometric technique (Boehler, 2000). The thermal emission emitted by the heated sample was analysed with a single-stage monochromator and collected on a cooled CCD detector. Temperatures were obtained by fitting the thermal radiation spectrum to Planck's function (Heinz and Jeanloz, 1987) in the entire visible spectrum (400 to 800 nm). The samples were quenched by mechanically blanking the laser beam, so as to provide ultra-high cooling rates. Pressures were measured at room temperature before and after heating using the ruby fluorescence technique, and averages were used as experimental pressures. Pressures and temperatures were chosen so as to describe a reasonable P–T path comparable to that of the Earth's mantle. Experimental conditions are summarized in Table 1.

2.2. Sample recovery by focused ion beam (FIB)

The samples recovered from the LH-DAC (about 40 μm large and 10 μm thick) were extracted from the rhenium gasket, glued onto carbon tape, and thinned to electron transparency (~100 nm) by the focused ion beam lift-out method. By sampling the thin section in the very center of the heated area, we minimized thermal gradients in the investigated area. FIB milling was performed with a FEI Model 200 TEM FIB system at CP2M (Marseille, France) following the extraction sequence presented in Fig. 1. A linear strap of platinum is deposited across the heated area, located by the imaging capabilities of the FIB, to protect the sample during the milling process. A 30 kV Ga^+ beam operating at ~20 nA is used to excavate a thin foil, removing sample material on both sides of the platinum layer to a depth of 5 μm. Before removal, the slide was further thinned

Table 1
Experimental conditions

Run	P (Gpa)	T (K)	Duration of heating [at peak T] (min)
Pv_08	55	2450	23 [18]
Pv_05	63	2450	11 [5]
Pv_04	72	2000	27 [9]
Pv_06	78	2200	11 [7]
Pv_13	100	2150	24 [11]
Pv_14	115	2200	7 [6]

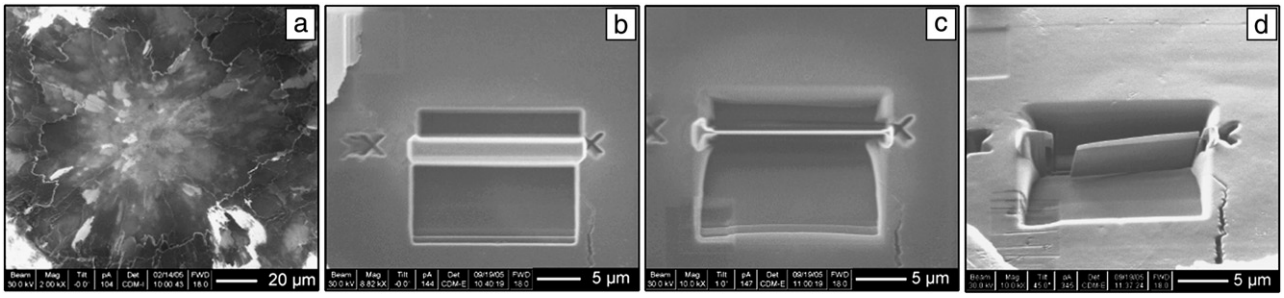

Fig. 1. Removal of a thin cross-section by the focused ion beam technique. a) Gallium ion image of the high-pressure recovered sample, b) a platinum layer protects the sample during ion milling, c) the foil is close to electron transparency (i.e., ~100 nm thick), d) once the required thickness is obtained, the foil is cut by the gallium beam and removed with a glass needle.

to ~100 nm with a glancing angle beam at lower beam current of ~100 pA. After cutting, the thin cross-section (15 μm× 5 μm×100 nm) is extracted by the electrostatic attraction of a glass needle and transferred onto a carbon-coated 200-mesh copper grid suitable for ATEM. Further description of the FIB sample preparation technique can be found in Heaney et al. (2001).

2.3. Analytical transmission electron microscopy (ATEM)

TEM observations were carried out on a JEOL 2010F microscope operating at 200 kV, equipped with a field emission gun and a high-resolution pole piece achieving a point-to-point resolution of 1.8 Å. Samples are inserted in the column with a double tilt specimen holder. Microstructures of the high-pressure phases were obtained by conventional electron imaging and diffraction. Quantitative chemical compositions were obtained on a Philips CM30 TEM operating at 300 kV equipped with an X-ray energy dispersive spectrometer (Noran-Voyager EDS) with a Ge detector and an ultra-thin window allowing detection of light elements with a good sensitivity. EDS was calibrated using a series of silicates and oxides. Moreover, we checked the iron, magnesium and silicon K factors using the starting San Carlos olivine. Analyses were recorded in the scanning transmission electron microscope mode (STEM) with typical total counts of 40,000. The concentrations were obtained using

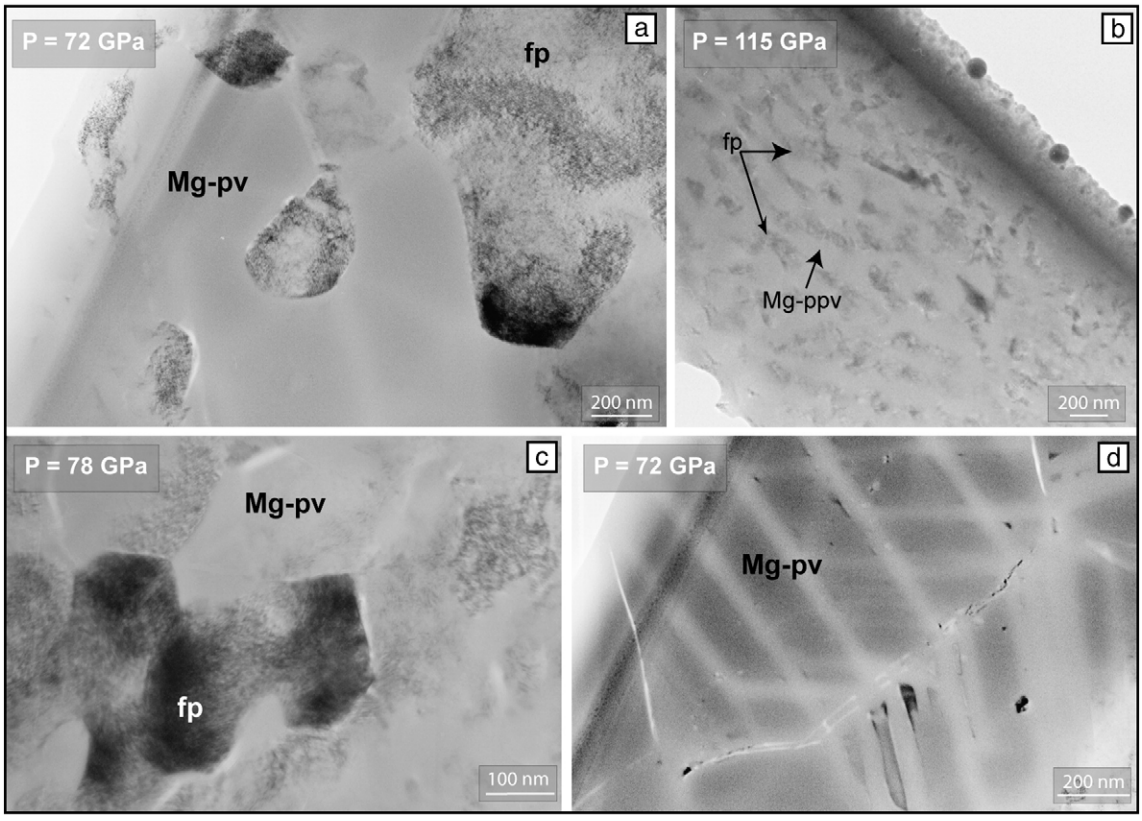

Fig. 2. TEM micrographs of mineralogical assemblages synthesized in a laser-heated diamond anvil cell at high pressures and high temperatures along the Earth geotherm. a) Amorphous pv and fp grains in Pv-04 synthesized at 72 GPa, b) same assemblage in a run conducted at 115 GPa, enlightening the pressure effect on the grain size, c) equilibrium texture in Pv-06, d) Amorphous pv showing the ghosts of the twin structures.

the method described by Cliff and Lorimer (1975). The FIB thin section generated thickness effects which require absorption corrections using the electroneutrality routine developed in van Cappellen and Doukhan (1994). As previously described by Carrez et al. (2001), the diffusion of chemical species adjacent to the electron spot leads to a marked change in the phase composition. This selective migration was corrected by the acquisition of temporal series (one spectrum every 10 s). The experimental values were obtained by fitting the elemental concentration *vs.* time curves with a first-order exponential function (see Supplementary material). Although elemental concentrations of fp are constant though time, pv is highly sensitive to the selective migration of elements under the electron beam.

2.4. Nanoscale secondary ion mass spectroscopy (nanoSIMS)

The nanoSIMS, a scanning ion microprobe, has secondary ion imaging capabilities of unprecedented spatial resolution (~100 nm with a O^- primary beam), and provides a powerful means for the chemical and isotopic characterization of our small-grained high-pressure phases. Indeed, it was recently shown (Badro et al., 2007) that the nanoSIMS allows the measurement of trace-element abundances in LH-DAC recovered samples at levels below 100 ppm. Analyses were carried out on a Cameca NanoSIMS 50 at Lawrence Livermore National Laboratory. A ~5 pA O^- primary beam was focused to a nominal spot size of ~200 nm and rastered over 256×256 or 128×128 pixel regions to generate secondary ions. Dwell time was 1 to 5 ms/pixel, and raster size was 3 to 5 μm square. The secondary mass spectrometer was tuned to a mass resolving power of ~4000 sufficient to resolve isobaric interferences for the elements of interest. Analysis was performed on five secondary ions suites [$^{24}Mg^+$, $^{28}Si^+$, $^{55}Mn^+$, $^{57}Fe^+$, $^{60}Ni^+$] in multi-collection mode by pulse counting on electron multipliers, generating 10 to 20 serial quantitative secondary ion images (layers) for each suite. Samples were also imaged simultaneously by secondary electrons detected by a photomultiplier. The data were processed as quantitative elemental ratio images using custom software. Secondary ion intensities were corrected for detector dead time and image shift from layer to layer, and normalised to magnesium.

For quantification, relative sensitivity factors (RSFs) were determined using the working curve in which the 24 Mg-normalised intensity of the isotopes of interest, ^{55}Mn, ^{57}Fe and ^{60}Ni, were obtained for samples of different compositions (ONLINE). Here we used a suite of standards prepared by Ionov et al. and Jochum et al. (2000) (that include geologically relevant compositions ranging from basalt to spinel to pyroxene to olivine).

3. Experimental results

We performed a set of experiments in the *P–T* range of the lower mantle (Table 1). Compared to recent studies of Fe–Mg exchange between the silicate and the oxide in the lower mantle, we worked at similar conditions as Murakami et al. (2005) but at

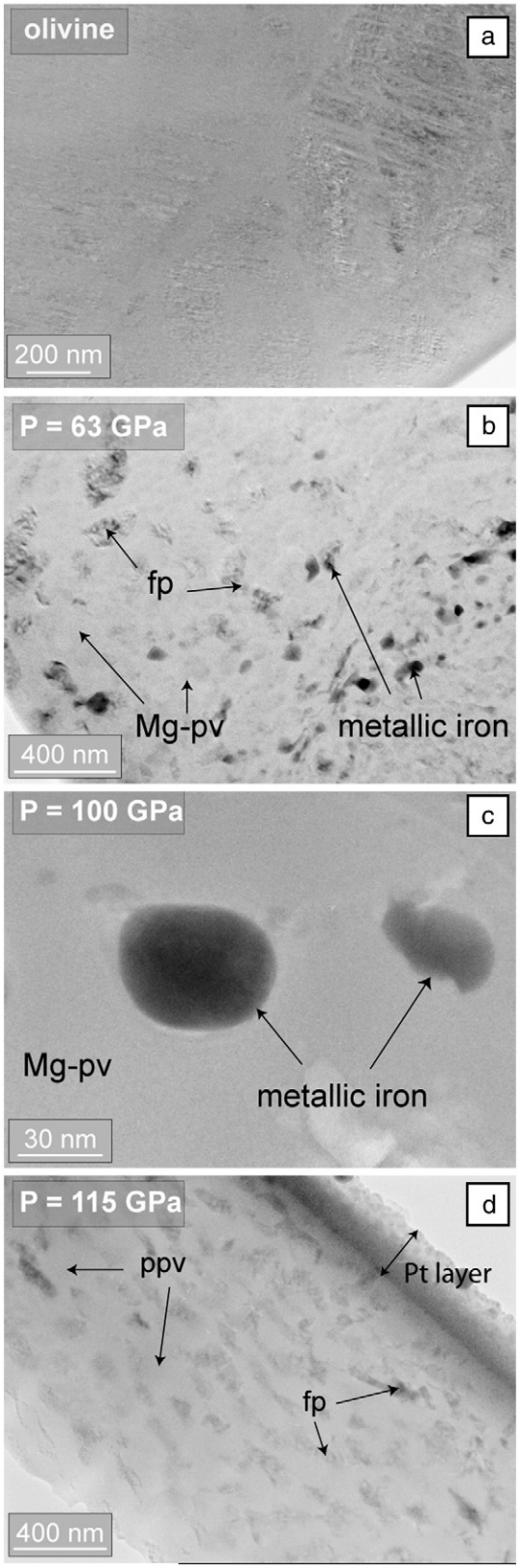

Fig. 3. Evidence of metallic iron in high-pressure experiments observed by transmission electron microscopy. a) The starting material does not contain a particle of metallic iron, b) and c) show magnesium silicate *perovskite* and *ferropericlase* coexisting in equilibrium with nanoparticles (a few tens of nanometers) of metallic iron. c) *Post-perovskite* and *ferropericlase* grains are observed without signs of metallic iron. The platinum (Pt) was deposited during the FIB thinning process to protect the sample during milling.

Table 2
Selected chemical composition of the high-pressure phases

	Pv-08		Pv-05		Pv-04		Pv-06		Pv-13		Pv-14	
	pv	fp	pv	fp	pv	fp	pv	fp	pv	fp	ppv	fp
Si	0.995 (9)	0.014 (1)	1.009 (11)	0.024 (3)	1.024 (8)	0.025 (4)	1.020 (11)	0.018 (5)	1.024 (13)	0.008 (2)	1.001 (14)	0.005 (1)
Mg	0.982 (15)	0.871 (12)	0.957 (17)	0.865 (8)	0.924 (10)	0.842 (7)	0.936 (16)	0.857 (13)	0.939 (22)	0.890 (17)	0.922 (19)	0.885 (15)
Fe	0.026 (1)	0.092 (2)	0.026 (1)	0.088 (2)	0.029 (1)	0.106 (3)	0.020 (1)	0.106 (5)	0.011 (1)	0.110 (5)	0.077 (4)	0.110 (5)
Mn	nd	nd	nd	nd	569 (85)	1829 (274)	nd	nd	1009 (302)	1743 (523)	921 (184)	1588 (317)
Ni	nd	nd	nd	nd	351 (53)	5891 (883)	nd	nd	99 (29)	5340 (1602)	2485 (497)	2474 (495)

Si, Mg and Fe are given in atoms per formula unit and Mn and Ni concentrations are given in ppm.

significantly higher temperature than Kobayashi et al. (2005). We were able to get very high-quality chemical analysis on only 6 samples out of the 12 synthesized. Indeed, a few slices were destroyed or lost during the FIB lift-out procedure. Moreover, we noted that grain size decreases with pressure to some extent (Fig. 2a and b), leading to samples poorly adapted to ATEM analysis (several grains in the thickness of the sample). Temperature increase also seems to affect the grain size, significantly reducing the average grain dimension from 600 nm (Pv_04, 2000 K) down to 200 nm (Pv_05, 2450 K) under similar pressure conditions.

TEM observations of the recovered samples displayed equilibrium textures even though ion milling blunts the edges due to preferential thinning at grain junctions (Fig. 2c). Bright field imaging combined with electron diffraction showed that in the high-pressure samples, the silicate was amorphous, probably due to ion milling. However, pv grains can easily be recognised due to the high concentration of twins that remain visible as "ghosts" after amorphization (Fig. 2d). This is attributed to the initiation of amorphization at the domain walls (Martinez et al., 1997). To our knowledge, there are no TEM observations of crystalline ppv due to the difficulty in quench recovery of this phase. Thus, we were not able to distinguish pv from ppv based on textural or X-ray observations. Based on the current phase diagram of pv/ppv [e.g. Hirose, 2006 for a review] we assume that the silicate was ppv before amorphization in sample Pv_14 which was confirmed by chemical analysis. In the samples successfully characterized by ATEM, the grain size ranges from 1 μm (Pv_04: 72 GPa) down to a few hundred nanometers (Pv_14: 115 GPa) (Fig. 2b). In all our experiments, the silicate appears as the interconnected phase, implying a strong control of the pv/ppv on the transport properties in the lower mantle.

We systematically observed small metallic nanoparticles (~ a few tens of nanometers) in all the pv–fp assemblages (Fig. 3b and c), but not in the ppv-bearing samples (Fig. 3d). The absence of metallic iron in the starting material (Fig. 3a) and in the ppv (Fig. 3d) proves that the particles are neither inherited nor experimental artefact. The dimension of these grains (about a few tens of nm) complicates the characterization but average chemical analysis coupled with the high absorption contrast observed in the TEM images, allows unambiguous identification of these particles as metallic iron grains. Indeed, chemical analysis of areas bearing several of these grains show a high concentration of iron coupled to a weaker oxygen peak. The O peak can be assigned to the surrounding matrix of pv and fp and is too weak to be accounted for by a distinct iron oxide, as opposed to metallic iron phase. The particles preferentially occur together with the pv grains (Fig. 3b and c) and represent about 1 vol.% of the sample. The occurrence of metallic grains has been reported previously (Frost et al., 2004) but also in several studies where high-pressure pv-bearing runs were investigated by high-resolution tools, the dimension of these particles precluding identification by X-ray diffraction (see Kobayashi et al., 2005).

We reported in Table 2 selected chemical analysis on (post-) perovskite and ferropericlase. We used chemical compositions measured on contiguous grains of pv (or ppv) and fp to calculate the exchange coefficients. Given the attainment of textural equlibirium, we assumed that contiguous grains reached chemical equilibrium. The Fe–Mg exchange coefficient

$$K^{\mathrm{pv-fp}} = (\mathrm{Fe/Mg})_{\mathrm{pv}}/(\mathrm{Fe/Mg})_{\mathrm{fp}}$$

is homogeneous within the entire foil, consistent with the attainment of chemical equilibrium. The value of $K^{\mathrm{pv-fp}}$ is

Table 3
Experimental results and exchange coefficients

Run	P (Gpa)	Grain size (nm)	Mineral assemblage	[a]Iron loss (%)	[b]$K_{\mathrm{Fe-Mg}}$	[c]$K_{\mathrm{Fe-Mg}}$	[c]$K_{\mathrm{Mn-Mg}}$	[c]$K_{\mathrm{Ni-Mg}}$
Pv_08	55	200	pv+fp+metal	42	0.24 (2)	nd	nd	nd
Pv_05	63	200	pv+fp+metal	38	0.27 (3)	nd	nd	nd
Pv_04	72	600	pv+fp+metal	30	0.23 (1)	0.30 (4)	0.73 (6)	0.08 (1)
Pv_06	78	300	pv+fp+metal	36	0.17 (2)	nd	nd	nd
Pv_13	100	300	pv+fp+metal	48	0.09 (1)	0.14 (2)	0.54 (13)	0.045 (2)
Pv_14	115	200	ppv+fp	9	0.66 (5)	0.55 (11)	0.77 (5)	0.48 (14)

[a] $[1-(\chi\mathrm{Fepv}+\chi\mathrm{Fefp})/\chi\mathrm{Feol}]*100$ (χ in molar fraction).
[b] $K=(\mathrm{Fe/Mg})\mathrm{pv}/(\mathrm{Fe/Mg})\mathrm{fp}$, the values in parentheses are the standard deviations.
[c] K is determined by nanoSIMS measurements.

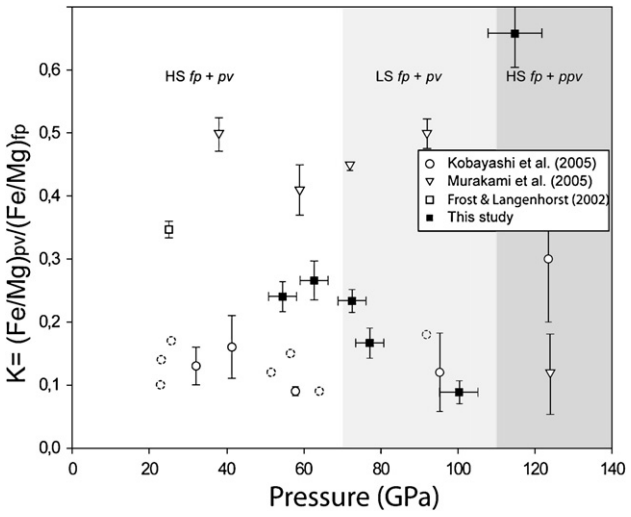

Fig. 4. Fe–Mg exchange coefficients between pv (or ppv) and fp plotted as a function of pressure. The coefficients published by Murakami et al. (2005) and Kobayashi et al. (2005) are reported for information. The three grey-shaded fields emphasize the stability fields of the successive coexisting phases: HS or LS fp+pv (Badro et al., 2003) and LS fp+ppv (Murakami et al., 2004).

systematically less than unity for all run conditions indicative of preferential partitioning of Fe, relative to Mg, into fp over the entire range of lower-mantle conditions (Table 3). However, significant variations of the exchange coefficient are observed in the investigated pressure range (Fig. 4). The exchange coefficient obtained in this study is relatively constant, ~0.2 up to 72 GPa. This strong partition of iron in the fp is consistent with recent investigations while slightly lower compared to Frost and Langenhorst (2002) who reported a partition coefficient at 0.35. It then gradually decreases between 72 and 100 GPa where it reaches a minimum at 0.09. At higher pressure, conditions relevant with the D″ layer, fp coexists with ppv, as shown by Murakami et al. (2004), and confirmed in the recent phase diagrams [e.g., Hirose, 2006 for a review]. At these pressures, the iron content in the silicate ppv sharply increases yielding an exchange coefficient K^{pv-fp} exceeding 0.6, much higher than any value measured between pv and fp. This Fe enrichment in the ppv phase is in agreement with Kobayashi et al. (2005) as shown on Fig. 4 while these authors reported a weaker iron enrichment in the ppv. Similarly, Mao et al. (2005) showed that iron-rich ppv (40 mol%), is likely to be stable at core–mantle boundary conditions, and could rather well satisfy the seismological observations. However, the iron content proposed by the latter authors is largely exceeding the one reported in our study.

The fact that iron is more compatible in the ppv phase compared to pv is also reinforced by the significant iron depletion (averaged around 35% relative to the initial content in olivine) observed in pv-bearing runs (Table 3) compared to the starting material (olivine). Iron loss is commonly observed in LH-DAC experiments due to chemical diffusion (Soret effect) in the thermal gradient. However, the magnitude of the depletion is beyond what would be expected from Soret effect in our configuration. This is further established by the fact that we observe much lower iron depletion in the oxide and silicate phases under similar heating conditions when ppv and fp coexist in the absence of a metallic phase. Frost et al. (2004) attributed the occurrence of iron-rich metallic particles in their experiments to disproportionation (or self-oxidation) of Fe^{2+} into $Fe^{3+}+Fe^{0}$ (metallic iron) in pv at fixed oxygen fugacity, and we observed such metallic grains in our perovskite-bearing runs. The depletion of iron in the silicate pv can therefore also be attributed to the self-oxidation of the perovskite phase coupled to Fe-metal precipitation. Our results show that this process can be extended to pressures up to a megabar, encompassing the entire lower mantle, exclusive of the D″ layer. Conversely, the absence of segregated metallic particles in the ppv-bearing assemblage coupled with negligible iron depletion in the oxide and silicate phases makes unlikely a similar Fe^{2+} disproportionation in ppv within the Earth. Finally, the high affinity of the ppv phase for iron seems robust.

NanoSIMS measurements were subsequently performed on the thin sections characterized by ATEM. After quantifying the chemical maps, we obtained Mg–Fe, Mg–Ni and Mg–Mn exchange coefficients. Fig. 5 shows the good agreement between the Fe–Mg exchange coefficients determined by EDX and by nanoSIMS. Manganese and nickel also preferentially partition into fp. Nickel is strongly depleted in the silicate while manganese shows a more moderate partitioning. Iron displays an intermediate behaviour. The pressure dependence of the Mg–Ni and Mg–Mn exchange coefficients also marks the transitions occurring at 70 and 110 GPa. Similar to the behaviour of iron, we observed an increasing depletion of Ni and Mn in pv between 70 and 100 GPa, and a dramatic increase of Ni and Mn concentration in ppv This shared behaviour was expected to accompany the phase transition, as iron, manganese and nickel share similar electronic and chemical properties. This was less likely concerning the spin-state transition of iron, as spin pairing is not possible for Ni due to its electronic configuration. On the other hand, Mattila et al. (2007) recently showed that Mn is likely to undergo a spin

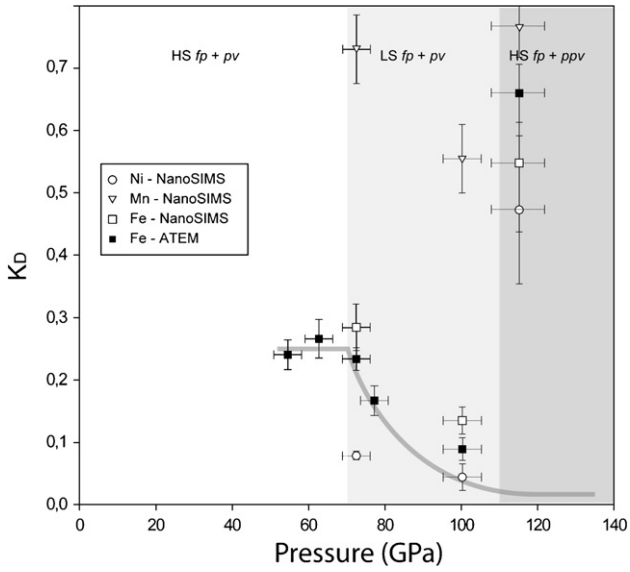

Fig. 5. Fe–Mg exchange coefficients determined by ATEM and nanoSIMS between pv (or ppv) and fp plotted as a function of pressure. The three grey-shaded fields emphasize the stability fields of the successive coexisting phases: HS or LS fp+pv (Badro et al., 2003) and LS fp+ppv (Murakami et al., 2004).

transition under conditions close to those of iron spin transition. This issue however deserves further investigation.

4. Discussion of the results

4.1. Iron partitioning under the lower-mantle conditions

Previous measurements of the Fe–Mg partitioning between lower-mantle phases has produced disparate results. The wide range of results can arise from the variability of starting compositions (iron content, presence of aluminium, oxidation state, among others), chemical characterization by indirect quantification methods (X-ray diffraction), or variations in P–T conditions. In this work, we compared EDX and nanoSIMS measurements and obtained similar Fe–Mg exchange coefficients between the silicate and fp. The preferential partitioning of iron into the fp demonstrated in this study is similar to that reported by several authors (Frost and Langenhorst, 2002; Kobayashi et al., 2005: Al-free system and Murakami et al., 2005: Al-rich system) (Fig. 4). Our average Fe–Mg exchange coefficient, ~0.2 for pressures up to 72 GPa is also in good agreement with that reported by Frost and Langenhorst (2002) for conditions relevant to the uppermost part of the lower mantle (25 GPa). However, at higher pressures, where the Fe spin-state transition occurs, the Fe–Mg exchange coefficient decreases, and we propose that this shift in the iron distribution between these two phases is related to this fundamental change in the chemistry of Fe. An enrichment of iron in the fp was predicted by crystal-field theory (Badro et al., 2003) and classical thermodynamic arguments (Badro et al., 2005) but has never before been observed experimentally (Kobayashi et al., 2005; Murakami et al., 2005). In this study, we report the first evidence of iron enrichment in fp and subsequent depletion in pv in the high spin–low spin (HS–LS) transition pressure range, evidence supported both by EDX and nanoSIMS measurements (Fig. 5).

Around 70 GPa, fp undergo a spin-pairing transition while iron in pv remains in the HS state. As LS iron atoms occupy a smaller volume compared to HS atoms, this transition should alter the chemical behaviour of the assemblage (Badro et al., 2005). Crystal-field theory (Burns, 1993) can provide estimates of the electronic contributions to enthalpy and entropy of HS and LS state. Based on these thermodynamic data, one can obtain the variation of the Gibbs free energy associated with the exchange reaction (1):

$$(Mg^{2+})_{fp} + (Fe^{2+})_{pv} \leftrightarrow (Mg^{2+})_{pv} + (Fe^{2+})_{fp} \quad (1)$$

At thermodynamic equilibrium, the equilibrium constant of reaction (1) (also referred as exchange coefficient K_D) is related to the change in Gibbs free energy G according to:

$$\ln(K_D) = \ln\left(\frac{X_{Fe}}{X_{Mg}}\right)_{fp} - \ln\left(\frac{X_{Fe}}{X_{Mg}}\right)_{pv} = -\frac{\Delta G}{RT} \quad (2)$$

where R is the universal gas constant, T the absolute temperature, and X the molar fractions.

A first-order Taylor expansion of the Gibbs free energy above the transition pressure yields:

$$\Delta G(P) = \{G_{LS}(P_{tr}) - G_{HS}(P_{tr})\} - \left\{\left(\frac{\partial G_{LS}}{\partial P}\right) - \left(\frac{\partial G_{HS}}{\partial P}\right)\right\} \cdot (P - P_{tr}) \quad (3)$$

where P_{tr} is the transition pressure and since $\frac{\partial G}{\partial P} = V$, Eq. (3) can be rewritten as follows:

$$\Delta G(P) = \{G_{LS}(P_{tr}) - G_{HS}(P_{tr})\} - \{V_{LS} - V_{HS}\} \cdot (P - P_{tr}). \quad (4)$$

At thermodynamic equilibrium, both LS and HS phases are in co-existence and $G_{HS}=G_{LS}$, thus the exchange coefficient can be rewritten from Eq. (2) as:

$$K = K_0.\exp\left(\frac{\Delta V \cdot (P - P_{tr})}{RT}\right) \quad (5)$$

where $K_0=0.25$ is the partition coefficient before the spin transition, $\Delta V=-1.39$ cm^3/mol is the volume difference between the HS and LS states (Badro et al., 2005). As shown on the diagram (Fig. 5), this simple model fits rather well with the experimental coefficients ($T=2500$ K an average temperature in the mid-lower mantle, $P_{tr}=70$ GPa the transition pressure). However it cannot account for the phase transition from pv to ppv, and does not explain the increase observed at 115 GPa.

This specific result relating the spin transition to the variation of the exchange behaviour observed here is at odds with Kobayashi et al. (2005) who systematically measured lower coefficients and observed no decrease above 70 GPa (Fig. 4). Both investigations used San Carlos olivine as starting material, constituting a simple Al-free system. What discriminates the two sets of data are the temperature conditions, our work being conducted at significant higher temperature conditions compared to Kobayashi et al. (2005) (1600 K). Frost and Langenhorst (2002) showed that it took at least 8 h to reach equilibrium in their 1650 °C experiments. Their K value increased with time until reaching a plateau value. One may wonder whether Kobayashi's experiments, which lasted a few tens of minutes at 1500 K and 1600 K, entirely reached equilibrium. Finally, the exchange coefficient is believed to increase with temperature (see Mao et al., 1997), which is concurrent with the comparison between the two investigations. High temperature effect also successfully explains the gradual depletion of iron in the pv in the spin-pairing domain as temperature increases the pressure range of the transition and create an intermediate domain where HS and LS iron are mixed (Sturhahn et al., 2005; Lin et al., 2007). You may also alternatively consider the coefficient from Frost and Langenhorst (2002) (Fig. 4) to propose that iron partitioning progressively decreases from low to high-pressure conditions in the stability field of pv. The iron enrichment in ppv above 110 GPa (Fig. 4) is less controversial, and is ascribed to the pv/ppv phase transition. While we observed the same tendency as Kobayashi et al. (2005), the iron enrichment is higher in our experiments likely due to similar temperature effects.

Valence state is likely to dramatically affect the (Mg,Fe) distribution between these phases, fp having a weak affinity for ferric iron. In an Al-bearing assemblage, Murakami et al. (2004) report a higher exchange coefficient (Fig. 4), meaning a more Fe-enriched pv phase. This could be a result of the high Fe^{3+} content commonly observed in Al-rich pv (McCammon, 1997; Lauterbach et al., 2000; Frost and Langenhorst, 2002; McCammon et al., 2004). On the other hand, the iron depletion observed in the silicate by Murakami et al. (2005) at the pv/ppv transition is not compatible with our results and those reported by Kobayashi et al. (2005). Indeed, they observe a more depleted ppv phase compared to pv, whereas this study and Kobayashi et al. (2005) show an iron-rich ppv phase. Further investigations of iron partitioning between fp and ppv in an Al-bearing system are needed to resolve this disparity. More precisely, it would be of prime importance to perform studies dealing with the effect of the oxidation state of iron on the partitioning of this element.

4.2. Geodynamical implications

Electronic and phase transitions can potentially affect the seismological signature and the dynamics of the lower mantle by altering the chemical and physical properties of the main lower-mantle phases and their modal proportions. Seismologically-observed complexity in the bottom 1000 km of the lower mantle leads to the idea of a deep layering (Wyesession et al., 1998; Kellogg et al., 1999) and leaves open the question of its origin. In this connection the coincidence of the seismological discontinuities in the inferred depths of mineralogical and petrological transitions can hardly be fortuitous. For instance, van der Hilst and Karason (1999) reported a change of the spatial pattern of heterogeneity between 1600 and 2000 km depth, that is in a pressure range compatible with the spin transition in iron-bearing ferropericlase (Badro et al., 2003). We have shown here that this transition is paired with significant iron depletion in the pv. Although the influence of iron content on the bulk modulus of pv and fp is weak (Kieffer et al., 2002; van Westrenen et al., 2005), it has a significant effect on the shear modulus of these phases. The iron depletion in the silicate should increase its shear modulus (Kieffer et al., 2002) while that of the fp should decrease due to its concomitant enrichment (Kung et al., 2002). At the same time, the spin pairing in ferropericlase, accompanied by a volume reduction, strongly affects the elastic properties of this mineral. Above 70 GPa, the bulk modulus and bulk sound velocity increase although no significant effect is observed on the density (Lin et al., 2005; Fei et al., 2007). Using a first approximation of the Birch-Murnaghan equation of state, we calculated the effect of the observed variation of iron partitioning above 70 GPa on the density of the assemblage pv+fp. Our results showed that no significant density variation is paired with the iron depletion in the silicate. We also expect an increase of the viscosity of pv due to iron depletion. Indeed, considering the rheological studies on olivine (Durham and Goetze, 1977; Zhao et al., 2005), the iron-depleted pv is potentially more viscous than an iron-bearing pv. Thus, while the single effect of shifting iron distribution cannot explain a deep dense layer as proposed by Kellogg et al. (1999), the coupled effects of iron partitioning (this study) and spin pairing (Badro et al., 2003, 2004; Lin et al., 2005) on the elastic and rheological properties have to be considered, the pressure range of the transition being consistent with the depth of the lower-mantle layering.

The D″ region, extending about 300 km above the CMB, is characterized by a complex pattern of increasing seismic velocities. This discontinuity coincides with the depth of transition from pv to ppv (Murakami et al., 2004). The physical properties of this phase satisfy rather well the seismic anomalies observed in this deep layer (see Hirose, 2006 for a discussion), leading to various scenarios involving ppv as a major component in this region (Lay et al., 2006; Mao et al., 2006; Spera et al., 2006; Yamazaki et al., 2006). While the three former authors consider that ppv can explain the increasing seismic velocities observed in the D″ layer, Mao et al. (2006) alternatively propose that an iron-rich ppv has the required properties to explain the seismological features of the ultra-low velocity zone close to the CMB. If our study agrees that ppv can accommodate larger amounts of iron compared to pv, the fp however remains the favourite host of this transition element. Our calculations showed that a fp+ppv assemblage with the iron concentration determined in this study is not significantly denser compared to the fp+pv assemblage (<0.5%). The variations of iron content in the lower-mantle phases coupled to the electronic and phase transitions have significant effects on the elastic and transport properties of these phases and should be included in thermochemical convection models. However, at first order, we argue that such variations should contribute to the layering of the mantle.

4.3. Metallic iron in the lower mantle

We have observed small particles of metallic iron in equilibrium with the pv+fp assemblage at high pressures (Fig. 3). Fe-metal precipitation is also evidenced by the fact that a significant part of iron is missing in the pv+fp assemblage (Table 3). Formation of Fe metal is not observed in fp+ppv assemblages suggesting that iron loss in the pv+fp assemblage is due to properties unique to pv. Frost et al. (2004) showed that under lower-mantle conditions, Fe^{2+} in pv disproportionates into Fe^{3+} and metallic iron (Fe^0). They assume that this process is due to a Fe^{3+}/Al^{3+} coupled substitution. We show here that aluminium is not mandatory for disproportionation. Indeed, Fe^{3+}/Fe^{3+} coupled substitution in the octahedral and dodecahedral sites can be responsible for high ferric iron content in Mg-pv as shown by Jackson et al. (2005) who performed a synchrotron mössbauer spectroscopic study on an Al-free pv. On the basis of iron depletion observed in their pv+fp assemblage at higher pressures, Kobayashi et al. (2005) suggested that this self-oxidation process could be extended into the deep mantle. Our study confirms that pv loses iron and segregates particles of metallic iron. The Fe-metal-free ppv-bearing assemblage produced at the highest pressure is also less depleted in iron (Table 3), indicating that Fe disproportionation or self-oxidation does not occur in this phase, which retains iron compared to pv. While there is no investigation of the oxidation state of iron in

an Al-bearing ppv available, we assume that disproportionation, if present, should be less important compared to Al-bearing pv. Interestingly, this means that the reaction of Fe disproportionation that occurs throughout the lower mantle, is stopped close to the core–mantle boundary. The ppv phase and the D″ layer where it would appear could thus be seen as a chemical buffer zone between the lower mantle and the core. Moreover, transport properties should dramatically change from a hot, conductive D″ layer where the connected ppv is iron-rich and the convecting mantle made of depleted pv. Influence on core–mantle boundary properties may be significant.

Wood et al. (2006) recently proposed that the pv self-oxidation reaction played a major role during core formation by: (i) internal generation of metal, that could be scavenged by descending metal diapirs carrying siderophile elements to the core and (ii) progressively increasing the oxidation state of the mantle/magma ocean thereby decreasing $D^{\text{metal-silicate}}$. This in turn reduces the discrepancy between the P–T conditions required to reconcile the siderophile abundance patterns and the peridotite liquidus. It would have taken about 20% self-oxidation of pv to explain present day abundances of Ni and Co in the mantle. It also reconciles the oxidation state of the current upper mantle. However, no mechanism was proposed to explain why the process may have stopped.

We propose, based on our observation that ppv does not self-oxidise and that the replacement of the pv by the ppv phase at the base of the mantle is the reason why that process stopped. However, one will keep in mind that for full demonstration, investigations of the ferric iron content in both pv and ppv have to be clearly establish. By chemically isolating the metallic core from the self-oxidising pv which then retains Fe metal in its assemblage, the stabilization of ppv phase could have locked in the oxygen fugacity of the mantle at that terminal point, and puts an end to core formation. We can then propose the following scenario. Early in the Hadean, during the stage of core formation, the Earth was still very hot, and the ppv phase was not stable at mantle pressures. The mantle consisted of only pv and fp, and the self-oxidation of pv could have contributed to core formation and mantle oxidation. When the Earth cooled, possibly at the late stages of core formation, and the temperature at the base of the mantle crossed that of the pv/ppv transition, ppv became stable (Hirose, 2006) and created a layer that isolated the core from the mantle, signalling the end of iron segregation into the core.

This process would also have considerably modified the interactions between the mantle and the core as the transport properties of an iron-rich and metal-free ppv layer should notably differ from that of a pv+Fe-metal particles bearing mantle. For instance, thermal conductivity variations have to be considered to infer heat flux and thus thermochemical models of the deep Earth. On a similar connection, electrical conductance of the D″ region is of prime importance for probing the core–mantle electromagnetic coupling (Brito et al., 1999).

4.4. Trace element partitioning under lower-mantle conditions

The nanoSIMS measurements, coupling a high spatial resolution (~100 nm) and a low detection threshold, provided high-quality analysis of trace elements on very small grains. Nickel and manganese display behaviour similar to iron. Indeed, all these elements are enriched in the fp, with exchange coefficients mimicking the variations observed for iron. This was expected as they all are transition elements. Moreover, Mattila et al. (2007) have shown that Mn can undergo a HS to LS transition at pressures close to that of iron. Now, variations of Ni can't be attributed to its HS–LS transition, as its electronic configuration does not permit it. Our results are in fairly good agreement with previous experimental determinations of exchange coefficients in the sense that $K_{\text{Mn}} > K_{\text{Fe}} > K_{\text{Ni}}$ (Kesson and Fitz Gerald, 1991; Malavergne et al., 1997; Martinez et al., 1997). The relative partitioning of the transition elements between the lower-mantle mineral associations has been proposed to be used as potential markers of the source region of deep diamonds [e.g. Kesson and Fitz Gerald, 1991]. Indeed, inclusions constituted of the "forbidden" assemblage $(Mg,Fe)SiO_3 + (Mg,Fe)O$ are considered to represent a lower-mantle equilibrium assemblage. The exchange coefficients experimentally determined between pv and fp fairly well explain the natural abundances in inclusions from diamonds collected in South Australia and South Africa (Kesson and Fitz Gerald, 1991), extending the pressure range of the potential origin of these diamonds close to the core–mantle boundary. Indeed, there is a pronounced preferential partitioning of Ni in the ferropericlase inclusions (Kd~0.1) and a moderate partition of Mn in this phase (Kd~0.5) which are consistent with our partitioning results. The pv/ppv transition significantly affects the distribution of the transition elements, particularly that of nickel, and can be considered as the bottom limit for deep diamonds origin. This could be used to eventually identify diamonds originating from the D″ region.

5. Conclusions

In this study, we have investigated transition element partitioning under lower-mantle conditions by a combination of nanoSIMS and ATEM measurements. We have shown that iron, manganese and nickel display a similar behaviour and favourably partition into fp and demonstrated that the spin transition of iron in fp affects the partitioning of iron between pv and fp, leading to an iron-depleted pv. At higher pressures relevant to the D″ layer, ppv accommodates large amounts of iron, nickel, and manganese. The effects of these coupled variations on the seismic velocities cannot be approximated without geophysical models, but it is of prime importance to populate these models with parameters considering the chemical effect of the spin transition and phase transition. However, at the first order, we propose that such variations should contribute to the layering of the mantle.

Observations of metallic iron in the pv+fp assemblages up to 110 GPa suggest that ferrous iron contained in pv disproportionates into ferric iron and metal. Thus, precipitation and dissolution of pv when the young Earth was large enough to produce this phase acted as a 'ferric iron pump', progressively oxidising the Earth. The appearance of a ppv layer at the CMB stopped this process and chemically isolated the convecting mantle and the outer core. Therefore, in modelling the processes

occurring in the deep mantle, it is important to consider these variations in the iron chemistry.

Considering the encouraging results obtained on samples synthesized above 100 GPa, the experimental platform comprising the LH-DAC, ATEM and nanoSIMS provides a powerful tool for high to ultra-high experimental petrology capable of competing against multi-anvil press. It opens a new field of investigations devoted to a better understanding of the lower-mantle geochemistry and dynamics.

Acknowledgments

This manuscript benefited from the helpful comments made by two anonymous reviewers. ALA thanks C. Vanni, C. Dominici and I. Raccourt from CP2M (Marseille) for the high-quality FIB thin sections. Support for this work was provided by the DyETI program, Institut National des Sciences de l'Univers (CNRS). The work is supported by the Laboratory Directed Research and Development Program operating under the auspices of the U.S. Department of Energy by the University of California, Lawrence Livermore National Laboratory, under contract No. W-7405-Eng-48.

Appendix A. Supplementary data

Supplementary data associated with this article can be found, in the online version, at doi:10.1016/j.epsl.2008.02.001.

References

Andrault, D., 2001. Evaluation of (Mg, Fe) partitioning between silicate perovskite and magnesiowustite up to 120 GPa and 2300 K. J. Geophys. Res. 106, 2079–2087.

Badro, J., Fiquet, G., Guyot, F., Rueff, J.-P., Struzhkin, V.V., Vanko, G., Monaco, G., 2003. Iron partitioning in Earth's mantle: toward a deep lower mantle discontinuity. Science 300, 789–791.

Badro, J., Rueff, J.-P., Vanko, G., Monaco, G., Fiquet, G., Guyot, F., 2004. Electronic transitions in perovskite: possible nonconvecting layers in the lower mantle. Science 305, 383–386.

Badro, J., Fiquet, G., Guyot, F., 2005. Thermochemical State of the Lower Mantle: New Insights from Mineral Physics. A. G. U. 241–260 pp.

Badro, J., Ryerson, F.J., Weber, P.K., Ricolleau, A., Fallon, S.J., Hutcheon, I.D., 2007. Chemical imaging with NanoSIMS: a window into deep-Earth geochemistry. Earth Planet. Sci. Lett. 262, 543–551.

Boehler, R., 2000. High-pressure experiments and the phase diagram of lower mantle and core materials. Rev. Geophys. 38, 221–245.

Brito, D., Aurnou, J., Olson, P., 1999. Can heterogeneous core–mantle electromagnetic coupling control geomagnetic reversals? Phys. Earth Planet. Inter. 112, 159–170.

Burns, R., 1993. Mineralogical Applications of Crystal Field Theory. Cambridge University Press, Cambridge. 551 pp.

Cappellen, E.v., Doukhan, J.-C., 1994. Quantitative transmission X-ray microanalysis of ionic compounds. Ultramicroscopy 53, 343–349.

Carrez, P., Leroux, H., Cordier, P., 2001. Electron-irradiation-induced phase transformation and fractional volatilization in (Mg,Fe)SiO_4 olivine thin film. Phil. Mag. 81, 2823–2840.

Cliff, G., Lorimer, G.W., 1975. The quantitative analysis of thin specimen. J. Microsc. 103, 203–207.

Dobson, D.P., Brodholt, J.P., 2000. The electrical conductivity of the lower mantle phase magnesiowustite at high temperatures and pressures. J. Geophys. Res.-Sol. Earth 105, 531–538.

Durham, W.B., Goetze, C., 1977. Plastic flow of oriented single crystals of olivine 1. Mechanical data. J. Geophys. Res. 82, 5737–5754.

Fei, Y., Zhang, A., Corgne, A., Watson, H., Ricoleau, A., Meng, Y., Prakapenka, V., 2007. Spin transition and equation of state of (Mg,Fe)O solid solutions. Geophys. Res. Lett. 34, L17307. doi:10.1029/2007GL030712.

Frost, D.J., Langenhorst, F., 2002. The effect of Al_2O_3 on Fe–Mg partitioning between magnesiowüstite and magnesium silicate perovskite. Earth Planet. Sci. Lett. 199, 227–241.

Frost, D.J., Liebske, C., Langenhorst, F., McCammon, C., Tronnes, R.G., Rubie, D.C., 2004. Experimental evidence for the existence of iron-rich metal in the Earth's lower mantle. Nature 428, 409–412.

Fujino, K., Sasaki, Y., Komori, T., Ogawa, H., Miyajima, N., Sata, N., Yagi, T., 2004. Approach of the mineralogy of the lower mantle by a combined method of a laser- heated diamond anvil cell experiment and analytical electron microscopy. Phys. Earth Planet. Inter. 143–144, 215–221.

Goncharov, A.F., Struzhkin, V.V., Jacobsen, S.D., 2006. Reduced radiative conductivity of low-spin (Mg,Fe)O in the lower mantle. Science 312, 1205–1208.

Heaney, P.J., Vicenzi, E.P., Giannuzzi, L.A., Livi, K.J.T., 2001. Focused ion beam milling: a method of site-specific sample extraction for microanalysis of Earth and planetary materials. Am. Mineral. 86, 1094–1099.

Heinz, D.L., Jeanloz, R., 1987. Temperature measurements in the laser-heated diamond anvil cell. In: Manghnani, M.H., Syono, Y. (Eds.), High-Pressure Research in Mineral Physics. Terra Scientific Publishing Co American Geophysical Union, Tokyo, pp. 113–127.

Hirose, K., 2006. Postperovskite phase transition and its geophysical implications. Rev. Geophys. 44.

Jackson, J.M., Sturnhan, W., Shen, G.Y., Zhao, J.Y., Hu, M.Y., Errandonea, D., Bass, J.D., Fei, Y.W., 2005. A synchrotron Mossbauer spectroscopy study of (Mg,Fe)SiO_3 perovskite up to 120 GPa. Am. Mineral. 90, 199–205.

Jackson, J.M., Sinogeikin, S.V., Jacobsen, S.D., Reichmann, H.J., Mackwell, S.J., Bass, J.D., 2006. Single-crystal elasticity and sound velocities of (Mg0.94Fe0.06)O ferropericlase to 20 GPa. J. Geophys. Res.-Sol. Earth 111.

Jochum, K.P., Dingwell, D.B., Rocholl, A., Stoll, B., Hofmann, A.W., Becker, S., Besmehn, A., Bessette, D., Dietze, H.J., Dulski, P., Erzinger, J., Hellebrand, E., Hoppe, P., Horn, I., Janssens, K., Jenner, G.A., Klein, M., McDonough, W.F., Maetz, M., Mezger, K., Munker, C., Nikogosian, I.K., Pickhardt, C., Raczek, I., Rhede, D., Seufert, H.M., Simakin, S.G., Sobolev, A.V., Spettel, B., Straub, S., Vincze, L., Wallianos, A., Weckwerth, G., Weyer, S., Wolf, D., Zimmer, M., 2000. Geostand. Newsl.: J. Geostand. Geoanal. 24 (1), 87–133.

Kellogg, L.H., Hager, B.H., Van der Hilst, R.D., 1999. Compositional stratification in the deep mantle. Science 283, 1881–1884.

Kesson, S.E., Fitz Gerald, J.D., 1991. Partitioning of MgO, FeO, NiO, MnO and Cr_2O_3 between magnesian silicate perovskite and magnesiowustite: implications for the origin of inclusions in diamond and the composition of the lower mantle. Earth Planet. Sci. Lett. 111, 229–240.

Kesson, S.E., O'Neill, H.S., Shelley, J.M.G., 2002. Partitioning of iron between magnesian silicate perovskite and magnesiowiistite at about 1 Mbar. Phys. Earth Planet. Inter. 131, 295–310.

Kieffer, B., Stixrude, L., Wentzcovitch, R.M., 2002. Elasticity of (Mg,Fe)SiO_3-perovskite at high pressures. Geophys. Res. Lett. 29.

Kobayashi, Y., Kondo, T., Othani, E., Hirao, N., Miyajima, N., Yagi, T., Nagase, H., Kikegawa, T., 2005. Fe–Mg partitioning between (Mg,Fe)SiO_3 post-perovskite, perovskite, and magnesiowüstite in the Earth's lower mantle. Geophys. Res. Lett. 32, L19301.

Kung, J., Li, B., Weidner, D.J., Zhang, J., Liebermann, R.C., 2002. Elasticity of ($Mg_{0.83}Fe_{0.17}$)O ferropericlase at high pressure: ultrasonic measurements in conjunction with X-radiation techniques. Earth Planet. Sci. Lett. 203, 557–566.

Lauterbach, S., McCammon, C., Van Aken, P.A., Langenhorst, F., Seifert, F., 2000. Mössbauer and ELNES spectroscopy of (Mg,Fe)(Si,Al)O_3 perovskite: a highly oxidised component of the lower mantle. Contrib. Mineral. Petrol. 138, 17–26.

Lay, T., Hernlund, J., Garnero, E.J., Thorne, M.S., 2006. A post-perovskite lens and D'' heat flux beneath the central Pacific. Science 314, 1272–1276.

Lin, J.-F., Struzhkin, V.V., Jacobsen, S.D., Hu, M.Y., Chow, P., Kung, J., Liu, H., Mao, H.K., Hemley, R.J., 2005. Spin transition of iron in magnesiowüstite in the Earth's lower mantle. Nature 436.

Lin, J.-F., Vanko, G., Jacobsen, S.D., Iota, V., Struzhkin, V.V., Prakapenka, V.B., Kuznetsov, V.B., Yoo, C.-S., 2007. Spin transition zone in the Earth's lower mantle. Science 317, 1740–1743.

Malavergne, V., Guyot, F., Wang, Y.B., Martinez, I., 1997. Partitioning of nickel, cobalt and manganese between silicate perovskite and periclase: a

test of crystal field theory at high pressure. Earth Planet. Sci. Lett. 146, 499–509.

Mao, H.K., Xu, J., Bell, P.M., 1986. Calibration of the ruby pressure gauge to 800 kbars under quasi-hydrostatic conditions. J. Geophys. Res. 91, 4763–4767.

Mao, H.K., Shen, G.Y., Hemley, R.J., 1997. Multivariable dependence of Fe–Mg partitioning in the lower mantle. Science 278, 2098–2100.

Mao, W.L., Meng, Y., Shen, G., Prakapenka, V.B., Cambell, A.J., Heinz, D.L., Shu, J., Caracas, R., Cohen, R.E., Fei, Y., Hemley, R.J., Mao, H.K., 2005. Iron-rich silicates in the Earth's D" layer. Proc. Natl. Acad. Sci. U. S. A. 102, 9751–9753.

Mao, W.L., Mao, H.K., Sturhahn, W., Zhao, J., Prakapenka, V.B., Meng, Y., Shu, J., Fei, Y., Hemley, R.J., 2006. Iron-rich post-perovskite and the origin of ultra-low velocity zones. Science 312, 564–565.

Mattila, A., Rueff, J.-P., Badro, J., Vanki, G., 2007. Metal-ligand interplay in strongly correlated oxides: a parametrized phase diagram for pressure-induced spin transitions. Phys. Rev. Lett. 98 N° 196404.

Martinez, I., Wang, Y.B., Guyot, F., Liebermann, R.C., Doukhan, J.C., 1997. Microstructures and iron partitioning in (Mg,Fe)SiO_3 perovskite (Mg,Fe)O magnesiowustite assemblages: an analytical transmission electron microscopy study. J. Geophys. Res.-Sol. Earth 102, 5265–5280.

McCammon, C., 1997. Perovskite as a possible sink for ferric iron in the lower mantle. Nature 387, 694–696.

McCammon, C., Lauterbach, S., Seifert, F., Langenhorst, F., Van Aken, P.A., 2004. Iron oxidation state in the lower mantle mineral assemblages. I. Empirical relations derived from high pressure experiments. Earth Planet. Sci. Lett. 222.

Murakami, M., Hirose, K., Kawamura, N., Sata, N., Ohishi, Y., 2004. Post-perovskite phase transition in $MgSiO_3$. Science 304, 855–858.

Murakami, M., Hirose, K., Sata, N., Ohishi, Y., 2005. Post-perovskite phase transition and mineral chemistry in the pyrolitic lowermost mantle. Geophys. Res. Lett. 32, L03304.

Spera, F.J., Yuen, D.A., Giles, G., 2006. Tradeoffs in chemical and thermal variations in the post-perovskite phase transition: mixed phase regions in the deep lower mantle? Phys. Earth Planet. Inter. 159, 234–246.

Sturhahn, W., Jackson, J.M., Lin, J.-F., 2005. The spin state of iron in minerals of Earth's lower mantle. Geophys. Res. Lett. 32, L12307.

van der Hilst, R.D., Karason, H., 1999. Compositional heterogeneity in the bottom 1000 kilometers of the Earth's mantle: toward a hybrid convection model. Science 283, 1885–1888.

Van der Hilst, R.D., Widiyantoro, S., Engdahl, E.R., 1997. Evidence for deep mantle circulation from global tomography. Nature 386.

van Westrenen, W., Li, J., Fei, Y., Frank, M.R., Hellwig, H., Komabayashi, T., Mibe, K., Minarik, W.G., Van Orman, J.A., Watson, H.C., Funakoshi, K.-I., Schmidt, M.W., 2005. Thermoelastic properties of $(Mg_{0.64}Fe_{0.36})O$ ferropericlase based on in situ X-ray diffraction to 26.7 GPa and 2173 K. Phys. Earth Planet. Inter. 151, 163–176.

Wood, B.J., 2000. Phase transformations and partitioning relations in peridotite under lower mantle conditions. Earth Planet. Sci. Lett. 174, 341–354.

Wood, B.J., Walter, M.J., Wade, J., 2006. Accretion of the Earth and segregation of its core. Nature 441, 825–833.

Wyesession, M., Lay, T., Revenaugh, J., Williams, Q., Garnero, E.J., Jeanloz, R., Kellogg, L.H., 1998. The D" discontinuity and its implications. In: Gurnis, M., Wyesession, M., Knittle, E., Buffet, B. (Eds.), The Core–Mantle Boundary Region 28. Geodynamics, Washington DC.

Yamazaki, D., Yoshino, T., Ohfuji, H., Ando, J.I., Yoneda, A., 2006. Origin of seismic anisotropy in the D'' layer inferred from shear deformation experiments on post-perovskite phase. Earth Planet. Sci. Lett. 252, 372–378.

Zhao, Y.H., Zimmerman, M., Kohlstedt, D.L., 2005. High temperature deformation experiment on iron rich olivine. Acta Petrol. Sin. 21, 999–1004.